Ocean Engineering 243 (2022) 110206

Contents lists available at ScienceDirect

Ocean Engineering

journal homepage: www.elsevier.com/locate/oceaneng

Hydrodynamic testing of wind-assisted cargo ships using a cyber–physical method

Thomas Sauder [a,b,*], Sverre A. Alterskjær [a]

[a] SINTEF Ocean AS, P.O. Box 4762 Torgarden, Trondheim, 7465, Norway
[b] Norwegian University of Science and Technology, Department of Marine Technology, Trondheim, 7491, Norway

ARTICLE INFO

Keywords:
Sail-assisted propulsion
Hydrodynamic testing
Cyber–physical empirical method
Bulk carrier
Rotor sail

ABSTRACT

A novel empirical method to study wind-assisted cargo ships is presented. The physical ship model, including propulsion units, interacts in real-time with a numerical sail model during free-running tests. Loads from the (virtual) sails are applied on the physical model using a cable-driven robot. All loads components except heave are applied with high accuracy and repeatability. The method is described thoroughly, and applied to investigate the benefits of wind assistance on a 190 m bulk-carrier, equipped with four rotor sails. Key performance indicators for wind assistance are established when sailing in steady wind profiles of various directions and velocities, and a propulsion analysis is performed. An important conclusion is that the increase of hydrodynamic resistance due to heel, leeway and rudder (that balance transverse sail loads) is rather limited for this ship, except when sailing close-hauled in strong winds. It is also demonstrated that experiments in a unsteady (virtual) wind environment can be successfully conducted. The effect of turbulence on the motions of this ship are found to be very limited. The conclusion discusses the other types of studies that can be enabled by this novel cyber–physical empirical method.

1. Introduction

While the idea of using wind assistance for the propulsion of modern ships dates back to the early 1900s (Tokaty, 1994), the wind-assisted propulsion devices have been receiving increased attention over the recent years (Lu and Ringsberg, 2020). This is mainly due to the increasing pressure for emission reduction and decarbonization of maritime sector (Council of the European Union, 2015). Fig. 1 presents the most recent, at the time of writing, new-built vessel equipped with 24-meter tall by 4-meter diameter rotor sails.

A vast number of research and development projects deals with traditional propelled vessels, aimed at hull and propulsion design optimization, friction reduction, alternative fuels, operation optimization, among others. In contrast, there is a knowledge gap in design, integration and operation of wind assisted propulsion in shipping. The physical complexity of the aerodynamics and hydrodynamics interaction of wind assisted ships are generally oversimplified, or neglected, to provide a performance prediction of a wind-assisted ship (Kramer et al., 2016). Indeed, the application of wind propulsion affects many aspects of the ship system as whole. (1) Wave patterns and hull resistance are modified and due to drift and heel angles, (2) Considerable hydrodynamic lift force and induced moment are generated by the hull due to drift (3) Appendage forces and rudder/propeller interaction are modified too, (4) Propulsion forces vary due to change of propeller loading and inflow angles, (5) The machinery system are affected through change of propulsion point (6) Roll and pitch damping increases due to the presence of sails which affects the added resistance in waves. (7) Inflow on bilge keels is considerably altered. Modeling each of these effects individually poses a challenge in itself, and so does the treatment of the coupling between the interacting effects (Tillig and Ringsberg, 2020).

Standards and procedures for performance prediction of vessels without wind propulsion through model tests are well established for a range of operational aspects. They are appropriately adopted for classification and verification of, for instance, EEDI-rating (ITTC Quality System Manual, 2017). However, there is a need for tailor-made empirical validation methods both as part of design optimization and final validation of new concepts comprising wind propulsion. In addition to classical ship model tests to study isolated effects such as hull, appendage and steering forces for a range of operating points relevant for a wind propelled vessel, integrated performance tests with free running ship models will necessitate the application of wind forces on the model. Ship model testing follows the Froude scaling laws to ensure a correct representation of wave systems. It is in practice impossible to fulfill Reynolds number similarity for wind propulsion systems at the same time, and this is a significant issue for e.g. Flettner

* Corresponding author at: SINTEF Ocean AS, P.O. Box 4762 Torgarden, Trondheim, 7465, Norway.
E-mail address: thomas.sauder@sintef.no (T. Sauder).

https://doi.org/10.1016/j.oceaneng.2021.110206
Received 30 June 2021; Received in revised form 28 September 2021; Accepted 13 November 2021
Available online 6 December 2021
0029-8018/© 2021 The Author(s). Published by Elsevier Ltd. This is an open access article under the CC BY license (http://creativecommons.org/licenses/by/4.0/).

Fig. 1. Very large ore carrier (VLOC) M/V Sea Zhoushan of the Brazilian mining company Vale, equipped with five rotor sails.
Source: Pictured in Zhoushan, China April 29, 2021. Credit photo: Vale

rotors and wing sails (Bordogna et al., 2019) Furthermore, there are technical challenges related to generation of a wind field (which ideally also could be dynamically changed during a test) around a moving object of appropriate quality in a hydrodynamic laboratory.

These issues are very similar to the ones that have been encountered in the early experimental studies of floating wind turbines, discussed in Bachynski et al. (2016) and Allen and Goupee (2017). For this application, poor wind field generation capabilities and Froude–Reynolds conflict have been solved by using a cyber–physical empirical method approach named "Real-Time Hybrid Model testing"[1](Sauder et al., 2016), instead of classical "fully-physical" experiments. In such a method, one part of the system is modeled physically, while the other part, whose behavior is assumed to be well described theoretically, is modeled numerically. Both physical and numerical substructures interact, in real-time, through a control system, composed of sensors, actuators, observers, allocation routines, etc. For floating wind turbines, ReaTHM testing enabled to study the dynamical behavior of large wind floating wind turbines (Thys et al., 2018, 2021), and put in evidence the effect of velocity-dependent eigenmodes that was then studied theoretically (S Souza et al., 2020). Back to the field of sail-assisted propulsion, advances have been made in the recent years in the numerical modeling of sails, based on analytical approaches (Tillig and Ringsberg, 2020), numerical studies (De Marco et al., 2016) and wind tunnel tests (Bordogna et al., 2019). See the review in Tillig and Ringsberg (2020) for details.

In the present paper, we present the first empirical study on sail-assisted ships using a cyber–physical approach, where wind loads, among others, are modeled numerically. We provide a detailed description of the proposed method, and present experimental results obtained during a pilot study performed in Mai 2021 in SINTEF Ocean's towing tank. In that study, a bulk carrier model retrofitted with four (virtual) Flettner rotor sails was freely running in the tank. Aerodynamic loads on the sails were computed in real-time based on the ship motions and on computational fluid dynamics results. These loads – all components except the heave force – were applied to the ship with high precision, closing the feedback loop. It is, to the authors' knowledge, an unprecedented contribution to the field of wind-assisted propulsion. The present paper is structured as follows. In Section 2, we first present the full-scale system that has been investigated, namely the vessel and the rotor sails and the wind environment. In Section 3, we detail the cyber–physical test setup that has been developed. The results of the test campaign are presented and analyzed in details in Section 4. Conclusions are drawn in Section 5.

[1] a.k.a. ReaTHM® testing, a registered trademark of SINTEF Ocean.

2. System description

2.1. SINTEF ocean bulk carrier (SOBC-1)

The concept of this ship is based on the idea of designing a benchmark vessel which is representative of the class of medium-size, medium range, single-screw tank/bulk carriers. The ship design features unconventional main dimensions originating from feasibility studies which have been conducted in the Centre for Research based Innovation (SFI) Smart Maritime (Anon, 2021) in 2019, and it implements state-of-the-art solutions regarding the hull lines, controllable pitch 4-bladed propeller and high-efficiency rudder designs. SOBC-1 is intended to serve as a testbed – physical and numerical – for various energy saving solutions and innovative "low-"/"zero-" emission technologies. In autumn 2020, the first hydrodynamic designs of the ship hull, propeller and rudder have been the result of joint effort between three research groups at SINTEF Ocean. This design version is based on the experience and current best practices, i.e. without heavy involvement of advanced numerical simulations. This ship type is highly relevant with respect to application of wind propulsors, and was therefore a natural choice of case vessel for this study. Main particulars are given in Table 2 and hull lines are presented in Fig. 2. Geometries of the hull, propeller, rudder and headbox will be made publicly available however are not published at the time of writing (see Fig. 3).

2.2. Flettner rotor sails arrangement

Rotor sails, commonly named Flettner Rotors after its 1920's inventor German aviation engineer Anton Flettner, are rapidly gaining interest. A number of installations are completed (see Fig. 1), and more are planned for RoRo/RoPax, product tankers, bulk carrier, among others. The Flettner rotor is a spinning vertical cylinder installed on the ship deck. The cylinder's rotational speed, provided by an electrical motor, combined with an incoming wind speed generates a lift force through the Magnus effect (Magnus, 1853), see Fig. 4. The lift force is perpendicular to the airflow, thus the maximum exploitation of the wind happens in apparent beam wind. When placing rotor sails on deck, care should be taken to avoid unfavorable interaction effects between rotors, as with all wind propulsion systems. Interaction effects between Flettner rotors in particular can according to Tillig and Ringsberg (2020) partly be compensated for by individual control of rotor RPM. Some comments and references will be provided in the next section.

The rotor sail design for SOBC-1 includes four rotor sails of height $H = 35$ m and diameter $d = 5$ m. All rotors are located on the ship's centerline. To ensure a minimum distance equal to the height of the rotor between adjacent rotor sails, rotors are equally spaced by 35 m. The aftmost rotor is located 30 m ahead of the aft perpendicular. Each rotor sail is fitted with a top end plate of $d_e = 6$ m diameter. Neglecting the effect of interaction and losses, this design should provide 90% of ship required thrust at a speed of 12 kn in 10 m/s wind with TWA = 110° (the reader is referred to the Nomenclature in Table 1 for the definition of terms, such as TWA, not explicitly defined in the text). The rotors are assumed to operate with a constant rotational speed of 180 rpm, i.e $\Omega = 18.9$ rad/s. No reefing, i.e. reduction of Ω during operations to reduce drag loads (Kramer et al., 2016; Tillig and Ringsberg, 2020), or thrust optimization strategy, is applied.

2.3. Wind field

In the present work, the wind field above deck is assumed to be described by an Atmospheric Boundary Layer modeled using a power

Table 1
Nomenclature. See also Table 2 for quantities related to vessel main particulars.

Symbol	Description	Unit	Support
AWA	Apparent wind angle (relative to bow)	^{o}	$[-180, 180]$
AWS	Apparent wind speed	m/s	$\mathbb{R}^+$
TWA	True wind angle (relative to bow)	^{o}	$[-180, 180]$
TWS, U_w	True wind speed	m/s	$\mathbb{R}^+$
TWD	True wind direction (relative to North)	^{o}	$[0, 360]$
COG	Course over ground	^{o}	$[0, 360]$
h	Height above deck	m	$\mathbb{R}^+$
C_D	Drag coefficient	–	$\mathbb{R}^+$
C_L	Lift coefficient	–	$\mathbb{R}^+$
AR	Aspect ratio	–	$\mathbb{R}^+$
H	Rotor height	m	$\mathbb{R}^+$
SR	Spin ratio	–	$\mathbb{R}^+$
d	Rotor diameter	m	$\mathbb{R}^+$
d_e	Rotor end-plate diameter	m	$\mathbb{R}^+$
Ω	Rotor rotational velocity	rad/s	$\mathbb{R}$
ρ_{air}	Air density	kg/m^3	$\mathbb{R}^+$
σ	Inverse Bellman coefficient	–	$\mathbb{R}^+$
$\{b\}$	Body-fixed coordinate system	–	–
$\{n\}$	Earth-fixed coordinate system	–	–
$\eta = (p, \Theta)$	Vessel pose[a]		
p	Vessel position[a] in $\{n\}$	m	$\mathbb{R}^3$
$\Theta = (\phi, \theta, \psi)^\top$	Vessel attitude (roll, pitch, yaw)[a] in $\{n\}$	rad	SO(3)
$\nu = (v^b, \omega^b)$	Vessel velocity[a] in $\{b\}$		
$\omega = (p, q, r)^\top$	Vessel angular velocity (roll, pitch, yaw)[a] in $\{b\}$	rad/s	$\mathbb{R}^3$
$v^b = (u, v, w)^\top$	Vessel linear velocity (surge, sway, heave)[a] in $\{b\}$	m/s	$\mathbb{R}^3$
τ	Load vector expressed in $\{b\}$	N	$\mathbb{R}^6$
T	tuple gathering line tensions	N	$(\mathbb{R}^+)^6$
J	Jacobian matrix	–	$\mathbb{R}^{6\times5}$ or $\mathbb{R}^{6\times6}$
r_i^b	Position of ith actuators's attachment point in $\{b\}$	m	$\mathbb{R}^3$
$p_{a,i}^n$	Position of ith actuators in $\{n\}$	m	$\mathbb{R}^3$
$r_{r,s}^b$	Position of the sth strip of the rth rotor in $\{b\}$	m	$\mathbb{R}^3$
ρ	Water density	kg/m^3	$\mathbb{R}^+$
n	Propeller rate of revolution	Hz	$\mathbb{R}^+$
D	Propeller diameter	m	$\mathbb{R}^+$
T_p	Propeller thrust	N	$\mathbb{R}^+$
Q_p	Propeller torque	Nm	$\mathbb{R}^+$
T_s	Thrust force from sails	N	$\mathbb{R}^+$
J, J_0	Advance coefficient	–	$\mathbb{R}^+$
K_{T_p}	Thrust coefficient	–	$\mathbb{R}^+$
K_{Q_p}, K_{Q_0}	Torque coefficient	–	$\mathbb{R}^+$
t, t^*	Thrust reduction fraction	–	$\mathbb{R}^+$
w	Wake fraction	–	$\mathbb{R}^+$
t, t^*	Thrust reduction fraction	–	$\mathbb{R}^+$
η_R	Relative rotative efficiency	–	$\mathbb{R}^+$
η_0	Propeller efficiency in open water	–	$\mathbb{R}^+$
η_H^*	Hull efficiency	–	$\mathbb{R}^+$
R_{Tm}	Hydrodynamic resistance without rotors	N	$\mathbb{R}^+$
R_{Tm}^*	Hydrodynamic resistance with rotors	N	$\mathbb{R}^+$

[a]See details in Section 3.

law with $\sigma = 9$ (inverse Bellman coefficient). The free-stream wind velocity $U_w(h)$ at a height h is given by

$$U_w(h)/U_w(h_0) = (h/h_0)^{\frac{1}{\sigma}} \tag{1}$$

The profile is presented in Fig. 5. Note that reference wind speed $U_w(h_0)$ is given at $h_0 = 20$ m so the wind speed on the upper part of the rotor sails are higher than $U_w(h_0)$. The wind shear (change of the TWD with the height), and the effect of the presence of the ship on the wind field have not been modeled in the present study. See e.g. Tillig and Ringsberg (2020) for a discussion about these effects in the context of sail-assisted propulsion.

Turbulent wind is modeled using the NPD (also known as Frøya or ISO spectrum) power spectrum:

$$S(f, z) = 3.2\ [U_w(h_0)]^2 \left(\frac{h_0}{10}\right)^{0.45} \left[1 + \tilde{f}^n\right]^{-5/(3n)} \tag{2}$$

where $n = 0.468$ and $\tilde{f}$ is

$$\tilde{f} = 172\ f\ \left(\frac{h_0}{10}\right)^{2/3} \left(\frac{U_w(h_0)}{10}\right)^{-3/4} \tag{3}$$

The associated 1-hour mean wind speed is

$$\bar{U} = U_w(h_0)\left[1 + 0.0573\sqrt{1 + 0.15\ U_w(h_0)}\ln\left(\frac{h_0}{10}\right)\right] \tag{4}$$

Fig. 5 shows three realizations with varying mean velocities, as well as their spectral content.

3. Experimental method

We will now describe in details the cyber–physical empirical method that has been developed to investigate the performance of this type of sail-assisted ships. The main components of the method will be successively presented, and a summary will be given at the end of the section.

3.1. Coordinate systems

Following the notations in Fossen (2011, Chapter 2), two frames of references are defined, one Earth-fixed that is denoted $\{n\}$, and one body-fixed that is denoted $\{b\}$. A coordinate system (B, b_1, b_2, b_3) is

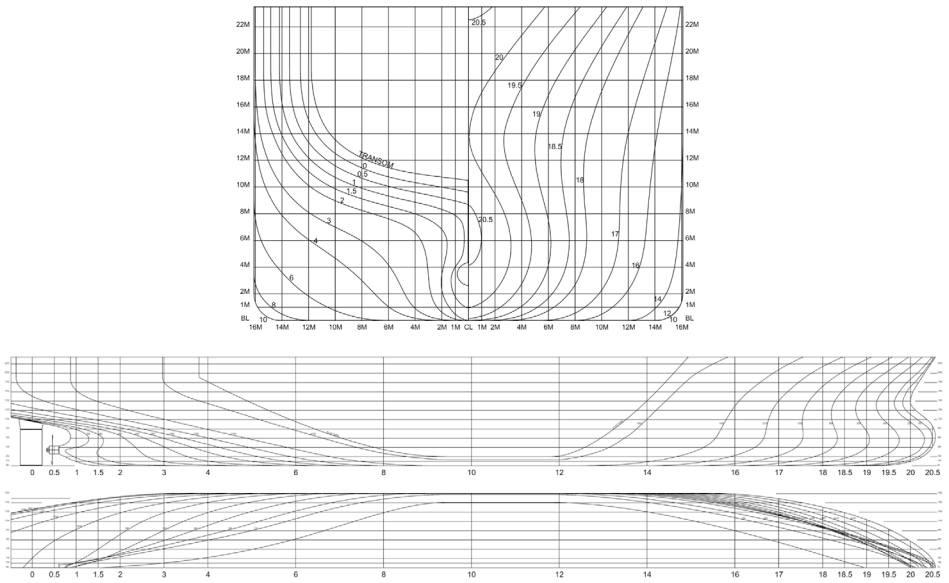

Fig. 2. SOBC-1 hull lines.

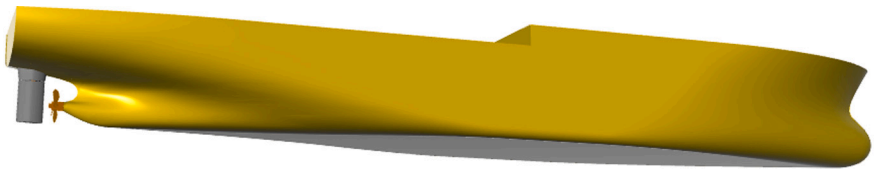

Fig. 3. SOBC-1 hull — 3D model.

Table 2
SOBC-1 main particulars at design waterline (DWL).

Parameter and symbol	Value
Length overall, LOA	200 m
Length betw. perp., LPP	190 m
Length on waterline, LWL	196.942 m
Breadth molded, B	32.295 m
Breadth waterline, BWL	32.201 m
Draught at FP/AP and LPP/2, T	11.000 m
Bilge radius	2 m
Wetted surface	8485.24 m^2
Wetted surf. of transom stern AT	2.91 m^2
Volume displacement ∇	48957 m^3
Prismatic coefficient (based on LPP), Cp	0.7308
Block coefficient (based on LWL), CBLW	0.7018
Propeller diameter, D	6.75 m
Pitch ratio at r/R = 0.7, $P/D_{0.7}$	0.970 –
Blade area ratio, A_E/A_0	0.483 –
Number of blades, Z	4 -
Chord/Diameter ratio, $c/D_{0.7R}$	0.3209 –
Thickness/Diameter ratio, $t/D_{0.7R}$	0.0324 –
Hub diameter ratio, d/D	0.252 –
Number of rotor sails, n_{rotors}	4
Rotor sail height, H	35 m
Rotor sail diameter, d	5 m
Rotor sail end-plate diameter, d_e	6 m
Rotor sail rotation velocity	180 rpm

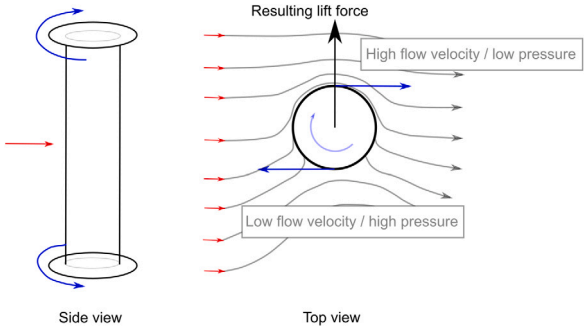

Fig. 4. Lift force generated by a Flettner rotor (black arrow), generated by the Magnus effect due to the interaction between incoming wind velocity (red arrows) and circumferential velocity (blue arrows). (For interpretation of the references to color in this figure legend, the reader is referred to the web version of this article.)
Source: Figure based on Pearson (2014).

attached to the ship, b_1 pointing forwards, b_2 towards starboard and b_3 downwards. The point B is located at mid-ship and, centerplane and deck level. $\{n\}$ and $\{b\}$ coincide when the ship is at rest.

The position and orientation of $\{b\}$ relative to $\{n\}$ are described by $p := p^n = (x, y, z)^\top \in \mathbb{R}^3$, the position of B, and $\Theta := (\phi, \theta, \psi)^\top$, the Euler (roll, pitch and yaw) angles. The body pose vector is $\eta := (p, \Theta)$. The body-fixed linear (surge, sway, heave) and angular (roll, pitch, yaw) velocities are denoted by $v^b = (u, v, w)^\top \in \mathbb{R}^3$ and $\omega^b = (p, q, r)^\top \in \mathbb{R}^3$, respectively. These are combined to form the body's linear and angular velocity vector $\nu := (v^b, \omega^b)$. The rotation matrix $R(\Theta) \in SO(3)$ and the angular velocity transformation matrix $T(\Theta)$ map vectors and angular velocities from $\{b\}$ to $\{n\}$:

$$R(\Theta) = R_z(\psi)R_y(\theta)R_x(\phi), \tag{5}$$

with,

$$R_x = \begin{pmatrix} 1 & 0 & 0 \\ 0 & \cos\phi & -\sin\phi \\ 0 & \sin\phi & \cos\phi \end{pmatrix}, \quad R_y = \begin{pmatrix} \cos\theta & 0 & \sin\theta \\ 0 & 1 & 0 \\ -\sin\theta & 0 & \cos\theta \end{pmatrix},$$

$$R_z = \begin{pmatrix} \cos\psi & -\sin\psi & 0 \\ \sin\psi & \cos\psi & 0 \\ 0 & 0 & 1 \end{pmatrix}, \tag{6}$$

leading to

$$R(\Theta) = \begin{pmatrix} \cos\psi\cos\theta & \cos\psi\sin\theta\sin\phi - \sin\psi\cos\phi & \sin\psi\sin\phi + \cos\psi\cos\phi\sin\theta \\ \sin\psi\cos\theta & \cos\psi\cos\phi + \sin\phi\sin\theta\sin\psi & \sin\theta\sin\psi\cos\phi - \cos\psi\sin\phi \\ -\sin\theta & \cos\theta\sin\phi & \cos\theta\cos\phi \end{pmatrix} \tag{7}$$

and

$$T(\Theta) = \begin{pmatrix} 1 & \sin\phi\tan\theta & \cos\phi\tan\theta \\ 0 & \cos\phi & -\sin\phi \\ 0 & \frac{\sin\phi}{\cos\theta} & \frac{\cos(\phi)}{\cos\theta} \end{pmatrix}. \tag{8}$$

Accordingly, the change of position in $\{n\}$ is given by $\dot{p}^n = R(\Theta)v^b$, and the change of attitude by $\dot{\Theta} = T(\Theta)\omega^b$.

3.2. Ship model in the seakeeping carriage

A model of SOBC-1 was designed at a scale $\lambda = 1/32$ and manufactured in wood, divinycell, and fiberglass coating. Neither bilge keels, nor tunnel thrusters were modeled for this experimental campaign. In order to obtain turbulent flow around the model, a trip wire is placed at station 19.5. A three-components accelerometer was fitted on deck, collocated with point B, and delivered data at frequency of 200 Hz. A three-components gyrometer was used to measured rotational velocity at the same frequency. An optical motion capture system was used to measure the ship position (relative to the towing carriage) and attitude at a frequency of 100 Hz. From these measurements, high-frequency, uninterrupted and unbiased estimates of η and ν were derived using the nonlinear observer described in Fossen (2011, Chapter 11).

The ship embedded a propulsion system (motor and propeller). Propeller thrust T_p and torque Q_p were acquired at 200 Hz. A controller was developed that could regulate either the rotational speed of the propeller, or the delivered power. In the latter case, power regulation was achieved by measuring the torque and adjusting the rotational speed of the propeller accordingly.

The experiments took place in SINTEF Ocean's towing tank that is 260 m long, 10.5 m wide and 10 m deep. The ship model was placed in the seakeeping carriage, as depicted in Fig. 6. Aerodynamic loads were applied on the ship through a stiff frame mounted on the ship's deck, and connected to six actuators mounted on the carriage. The loads were applied on the frame through six thin wires visible in Fig. 6. The tension in the wires was measured at a frequency of 200 Hz. More details about aerodynamic load actuation will be given in the following subsections.

3.3. Computation of sail loads

Sail loads were computed by a quasi-steady approach and a strip theory. Representative drag and lift coefficients for each rotor are derived based on Computational Fluid Dynamics (CFD) presented in De Marco et al. (2016). Each of the four rotors were modeled by $n_{\text{strips}} = 11$ strips of constant height $\Delta H = 3.18$ m each. The apparent wind angle (AWA) and apparent wind speed (AWS) were assumed to be constant on each strip, but did vary between strips due to the wind profile and the ship motions. The interaction between rotor sails was neglected, which is a valid assumption in apparent beam wind conditions, but becomes questionable close to head wind (AWA$\rightarrow 0°$) and tail wind (AWA$\rightarrow$ 180 deg) conditions (Garzón and Figueroa, 2017; Bordogna et al., 2019; Tillig and Ringsberg, 2020).

De Marco et al. (2016) performed a parametric study with CFD aimed at establishing the drag and lift coefficients on various rotor sails geometries operating at various rotational speeds. They solved the unsteady Reynolds-averaged Navier–Stokes equations and used a $k-\omega$ Shear Stress-Transport turbulence model. The size of the computational grid was in the order of 1.3 million cells. Based on the CFD results, lift and drag coefficients were approximated as a multivariate polynomial function of the aspect ratio $AR = d/H$, normalized end-plate diameter d_e/d, and spin ratio $SR = \frac{\Omega d/2}{U_w}$:

$$C_L = \sum_{i=1}^{4}\sum_{j=1}^{4}\sum_{k=1}^{3} a_{ijk}(SR)^{i-1}(AR)^{j-1}(d_e/d)^{k-1} \tag{9}$$

and

$$C_D = \sum_{i=1}^{4}\sum_{j=1}^{4}\sum_{k=1}^{3} b_{ijk}(SR)^{i-1}(AR)^{j-1}(d_e/d)^{k-1} \tag{10}$$

where the polynomial coefficients a_{ijk} and b_{ijk} are provided in Table A.5 in Appendix.[2]

In the present case, $d_e/d = 1.2$ and $AR = 7$ was used throughout, as these values represent dimensions close to existing commercial Flettner Rotor applications, while SR varied depending on the wind and speed condition. Fig. 7 presents the lift and drag coefficients as a function of SR. When SR exceeded the validity range of the polynomial fitting ($SR \in [1, 3]$), the closest values of lift and drag coefficients were used. One should be aware that (De Marco et al., 2016) reports uncertainties on the order of 20%–40%, particularly for C_d, and especially at large SR ranges (> 2).

Following a strip-theory approach, for each strip $s \in \{1, \dots, n_{\text{strips}}\}$ of rotor $r \in \{1 \dots n_{\text{rotors}}\}$, the AWS and AWA were evaluated from $U_w(h)$, η and ν, and the aerodynamic lift and drag forces (denoted f_L and f_D) were computed by

$$f_{L,D}(r,s) = \frac{1}{2}\rho_{\text{air}} \cdot C_{L,D}(AR, SR, d_e/d) \cdot d \cdot \Delta H \cdot (AWS)^2. \tag{11}$$

where $\rho_{\text{air}} = 1$ kg/m^3. Using the AWA for each strip, the aerodynamic force vector $(f_L(r,s), f_D(r,s))$, orthogonal to the rotor's main axis, was then expressed in the body-fixed coordinate system, leading to a strip force $(f_1(r,s), f_2(r,s), 0)$ in $\{b\}$. The load global load from the sail was then found by summation over the n_{strips} strips and n_{rotors} rotors.

$$\tau_{\text{sail}} = \sum_{r=1}^{n_{\text{rotors}}}\sum_{s=1}^{n_{\text{strips}}} \begin{pmatrix} (f_1(r,s), f_2(r,s), 0)^\top \\ r^b_{r,s} \times (f_1(r,s), f_2(r,s), 0)^\top \end{pmatrix} \tag{12}$$

where $r^b_{r,s}$ denotes the coordinates of the geometric center of the sth strip of rotor r, in the local coordinate system $\{b\}$. Note that the present approach intrinsically includes the de-powering of the sails when the vessel is heeling, as some of the incoming flow velocity vector is projected on the rotor axis, and does hence not contribute to the lift and drag force calculations. The fact that heeling of the vessel combined with sail forces induces a yaw moment is also intrinsically modeled.

3.4. Additional loads applied on the ship

As the full-scale and model-scale Reynolds number differ, the frictional resistance of the model and the frictional resistance of the ship converted to model scale, are different. The latter being less than the former, it implies that the model should be unloaded with a "towing" force in the direction of motion to compensate for this scale effect.

$$\tau_{\text{friction},1} = C_s \frac{\rho_m}{2} V_m^2 S_m \tag{13}$$

where C_s is determined by the difference in frictional resistance (as per the ITTC-1957 frictional correlation line), base drag and roughness allowance between the model and the full scale ship. For details it is referred to procedures outlined in the ITTC (ITTC Quality System Manual, 2017) Inserting numbers, the friction correction is approximated as:

$$\tau_{\text{friction},1} = 5.484 \cdot u^2 + 17.492 \cdot u \text{ [kN]} \tag{14}$$

[2] Note that the coefficients reported in De Marco et al. (2016) lacked significant digits and led to significant inaccuracies in the polynomial approximation. Coefficients with sufficient precision have been obtained in private communication with the authors, which are the ones reported in Table A.5.

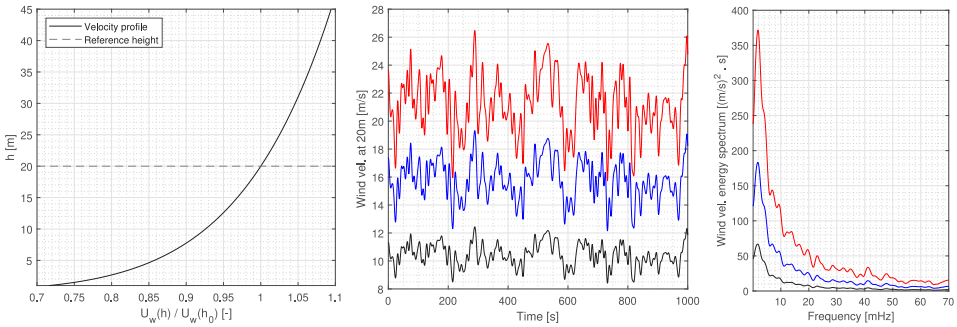

Fig. 5. Wind field properties. Left: Wind velocity profile (used both for constant and turbulent wind at all wind speeds). Middle/Right: turbulent wind times series and energy spectrum for mean wind velocities of 10.6 m/s, 16.1 m/s and 21.6 m/s.

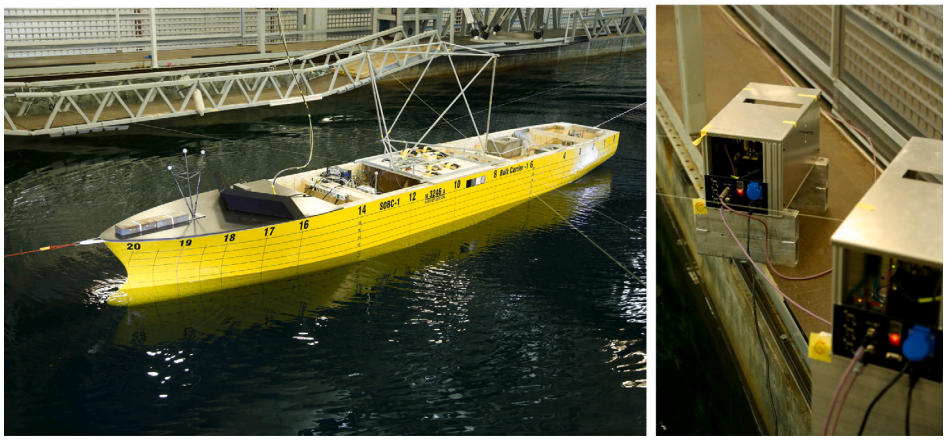

Fig. 6. Model of SOBC-1 in the towing tank (left). Two of the six actuators mounted on the carriage (right). Thin lines connecting the model to the actuators are visible on both figures.

which leads for example to a force of about 9.54 N at model scale for a vessel speed of 12 kn (full-scale).

Wind loads on the ship superstructure (except sails) were assumed to be representative at model scale, and no correction was applied to them.

Finally, as no bilge keels were fitted to the model, an additional roll damping load was applied for convenience to reduce transients

$$\tau_{\text{roll-damping},4} = 190 \cdot r \ \text{[kNm/(deg/s)]} \tag{15}$$

The external load to be applied to the ship (in addition to hydrodynamic resistance and propulsion loads) was then

$$\tau = \tau_{\text{sail}} + \tau_{\text{friction}} + \tau_{\text{roll-damping}} \tag{16}$$

3.5. Load actuation on the vessel model

The load given in (16) was applied to the vessel by a cable-driven parallel robot (CDPR) developed at SINTEF Ocean. The CDPR consisted of a set of six actuators mounted on the seakeeping carriage, each connected with a cable to the ship tested. More details about the CDPR can be found in Ueland et al. (2020) and Ueland et al. (2021).

For each actuator $i \in \{1, \dots, 6\}$, let $p_{a,i} := p^n_{ai}$ be the fixed position of the ith actuator A_i on the carriage. Similarly, let E_i the ith attachment point of the corresponding line on the ship. The constant vector r^b_i expressed in $\{b\}$ describes the position of E_i with respect to B. It follows that the absolute position of E_i with respect to the carriage is $p_{e,i} := p^n + R(\Theta) r^b_i$. From each actuator i, a force f_i is acting on the platform at E_i, directed along the unit vector $u_i := \frac{p^n_{a,i} - p^n_{e,i}}{|p^n_{a,i} - p^n_{e,i}|} \in \mathbb{R}^3$. The relationship between the vector gathering the cable tension $T \in \mathbb{R}^6$ and

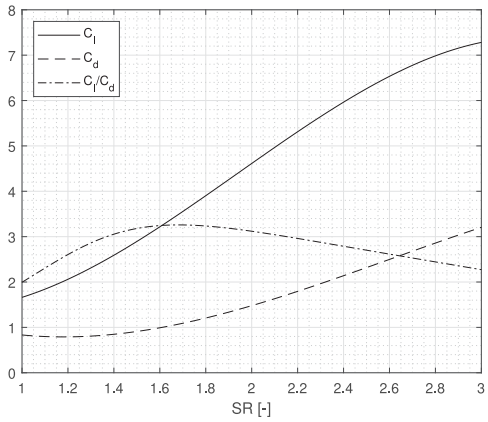

Fig. 7. Lift and drag coefficients for the rotor sails used in the present study.

the load vector $\tau \in \mathbb{R}^6$ applied by the cables is given by

$$\tau = JT \tag{17}$$

where

$$J = \left[q_1 q_2 \cdots q_n\right], \ \text{with} \ q_i = \begin{bmatrix} u_i \\ r^b_i \times u_i \end{bmatrix}. \tag{18}$$

Note that J varies in time due to variations of the pose of the ship in the carriage. The actuator configuration is fully described by $\{p_{a,i}\}_{i=1\dots6}$ and $\{r^b_i\}_{i=1\dots6}$, which are given in Table 3 and Fig. 8 for the present setup.

Tension *allocation* consists in choosing a set of positive cable tensions T such that the resulting load $\tau = JT$ matches the desired

Table 3
Actuator placement [m, full-scale]. See Fig. 8.

i	$p^n_{a,i} \cdot n_1$	$p^n_{a,i} \cdot n_2$	$p^n_{a,i} \cdot n_3$	$r^b_1 \cdot b_1$	$r^b_2 \cdot b_2$	$r^b_3 \cdot b_3$
1	102.40	167.36	−32.00	−18.01	10.40	−35.20
2	144.00	167.36	−22.40	19.55	−7.11	−3.20
3	−292.80	−22.08	−26.88	−3.61	−20.48	−35.20
4	−292.80	20.80	−26.88	−3.61	20.48	−3.20
5	144.00	−167.36	−32.00	19.55	7.11	−35.20
6	102.40	−167.36	−22.40	−18.01	−10.40	−3.20

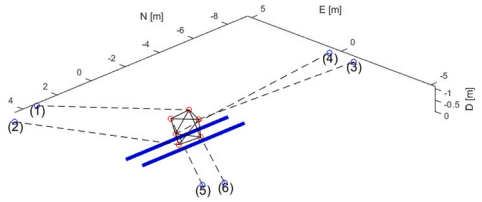

Fig. 8. Placement of the actuators and attachment points. The Figure has a similar orientation as Fig. 6. Actuator numbering in parentheses. The blue thick lines represent the sides of the ship's deck. Coordinates are at model scale. (For interpretation of the references to color in this figure legend, the reader is referred to the web version of this article.)

reference load τ_{ref} given by (16). Here the allocation problem is cast as follows:

$$T^* = \arg\min_T \sum_{i=1}^{n} (T_i - T_0)_i^2 \text{ subject to } \quad JT = \tau_{\text{ref}} \tag{19}$$

where $T_0 > 0$ is a preferred tension. In other words, we wish to minimize deviations from a preferred tension, typically 20 N in our case. A direct solution can be obtained by $T_i - T_0 = J^\dagger(\tau_{\text{ref}} - JT_0)$ where $J^\dagger$ is the Moore–Penrose matrix inverse, a type of pseudo-inverse. In practice, τ_{ref} and J are provided discretely at each time step, meaning that Eq. (19) will be solved in each time-step. In that context, the iterative method of Ben Israel and Cohen is an efficient way of computing $J^\dagger$, starting from the estimate of $J_i^\dagger$ from the previous time step.

$$J_{i+1}^\dagger = 2J_i^\dagger - J_i^\dagger J J_i^\dagger \tag{20}$$

Note finally that in the present case, we do not attempt to *control* the third component of τ (heave force), meaning that the dimensions of J is reduced to 5×6 when solving the allocation problem. Given the measured cable tensions T, we can however compute *measure* the spurious heave force that was actually applied. It amounted typically to 4–5 N directed upwards and applied approximately at midship. This contribution is insignificant compared to buoyancy and inertia forces in heave. It did not cause any observable change of sinkage/trim either, given the large water-plane area stiffness of the vessel. A thorough description of the force controller for each individual actuator has been given in Ueland et al. (2021) and is not repeated here.

3.6. Typical test procedure

Fig. 9 presents a block diagram of the closed loop system described in this section. The loop time was of 5 ms. A typical test procedure was as follows. At the beginning of each test, the vessel propeller was activated and the model kept in position using two ropes attached at the bow and stern, respectively, which are visible in Fig. 6. The carriage was then accelerated to a speed that was estimated to be the likely final speed of the vessel for this test condition. Shortly after this carriage speed was achieved, the model was released, i.e. the bow and stern lines were slackened, and the model was freely running.

An autopilot acting on the rudder was ensuring that the ship origin B remained on the centerline of the towing tank. It is worth emphasizing that the autopilot was not ensuring a zero yaw angle/heading, but a zero Course Over Ground (COG). The carriage velocity was then controlled so that the carriage transverse platform remained at a constant distance ahead of the free-running model. Steady-state was reached, including application of external forces with the CDPR. When the tank length was about to be covered, bow and aft lines were tightened to control the ship, and the carriage was slowed down. The quantities of interest for the tests (presented in the next section) were obtained by time-averaging after that steady-state has been reached.

4. Results and analysis

The test campaign took place between the 15th and 22nd of May 2021 in SINTEF Ocean's towing tank. Several types of free-running tests were performed: (1) test without sails, (2) tests in steady wind conditions with varying TWD and TWS, (3) tests in turbulent wind, and (4) tests in steady beam wind conditions aimed at assessing the repeatability of the method described in Section 3, Each set of tests will be presented in the following subsections.

4.1. Free running tests without sails

The first objective was to establish the key propulsion parameters when operating (without wind) at various speeds. To this end, the propeller was controlled to achieve a constant RPS. The only load applied to the ship by the CDPR was τ_{friction}, i.e. the surge force correcting for friction at model scale. Five tests were run, with targeted vessel speed from 10 kn to 18 kn (at full-scale), by steps of 2 kn. Time series for these runs are superimposed in C.17 (Appendix). The reduced data obtained from time-averaging of the last 150 s of the time series is presented in Fig. 10.

For further propulsion analyses, a third-order polynomial fit of the propeller thrust T_0 [kN] and power P_0 [kW] obtained in these "sail-free" conditions as a function of the vessel speed u [m/s] was established:

$$T_0(u) = \sum_{i=0}^{3} \alpha_i u^i \text{ with } \alpha_0 = 37.2, \alpha_1 = 80.6, \alpha_2 = -21.3, \text{ and } \alpha_3 = 3.0 \tag{21}$$

$$P_0(u) = \sum_{i=0}^{3} \alpha_i u^i \text{ with } \alpha_0 = -6211.1, \alpha_1 = 4518.7, \alpha_2 = -991.4 \text{ and } \alpha_3 = 80.2 \tag{22}$$

The polynomial fits are presented together with the thrust and power curves in Fig. 10. Note finally that the desired load τ_{friction} and the load applied by the CDPR agree very well, as seen by comparing the red and black curves in Fig. C.17.

4.2. Tests with rotor sails - Preliminaries and repeatability

Free-running tests were then performed with wind loads as described in Section 3. To assess the repeatability of the method, seven identical tests were conducted at random times throughout the test week. They consisted of tests in a steady wind profile, with TWS = 10 m/s, at a reference height of 20 m above the free-surface (see Fig. 5). The TWD was 90°, meaning beam wind coming from the starboard side of the ship. The ship propulsion unit was controlled to deliver a power of 3078 kW which corresponded to the required power to achieve 12.25 kn (full-scale) without wind nor sails. Time series of the seven tests are superimposed in Fig. C.18. Time series were synchronized by setting the origin of time to the instant when the vessel forward velocity exceeded 2 m/s. The reduced data was obtaining by time-averaging the last 150 s of the time series.

Statistical properties for the reduced data are presented in Table 4. They include mean values (over the 7 runs), standard deviation, and coefficient of variation (CoV) that is the ratio between standard deviation and mean. In general, all CoV values are below 1%. Exceptions are

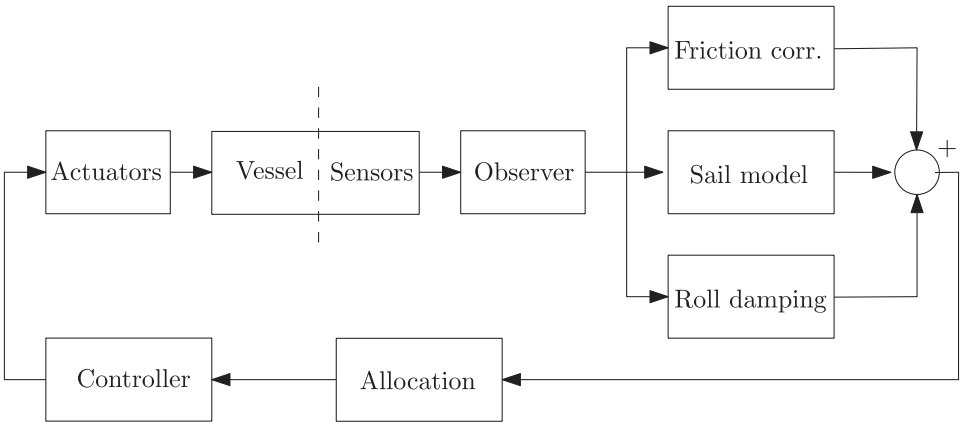

Fig. 9. Block diagram Control system.

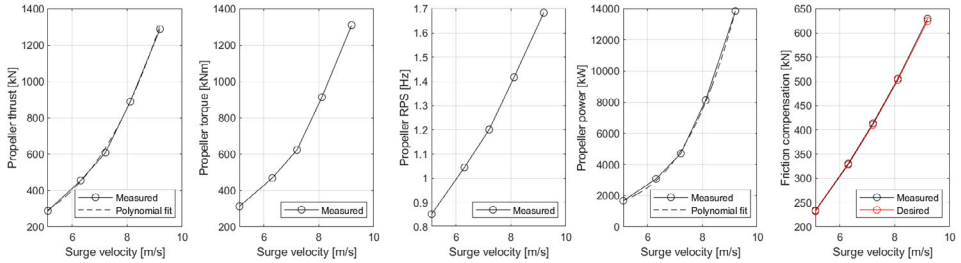

Fig. 10. Key propulsion parameters for runs at various velocities without wind.

quantities with for which the mean values are close to zero, leading to an artificially large CoV, even if the standard deviation is small. This is the case for the heel, trim and yaw angles. Larger CoVs are observed for the propeller thrust (2.2%) and rudder angle (2.5%), and which are due to autopilot acting on the rudder to achieve COG = 0°, i.e. ship origin staying long the mid-axis of the towing tank.

The desired and achieved loads applied by the CDPR (when both friction compensation and wind loads are applied) were also compared. Based on the measured velocities and position/attitude, the target surge force was computed as $\tau_{\text{sail},1} + \tau_{\text{friction},1}$, with mean value of 192.64 kN + 429.56 = 622.20 kN, while the measured surge force applied by the CDPR is 626.49 kN, i.e. a 0.69% deviation. As a conclusion, the repeatability the key quantities, and accuracy of the applied loads was excellent for this representative test

4.3. Tests in constant wind of varying speed and angle

Free running tests were performed in steady wind profiles from various directions and velocities. The test matrix consisted in variations of TWD from 30° (close hauled, near head wind) to 150° (broad reach, close to downwind) by steps of 20°, while and TWS varied between 10, 15, and 20 m/s. Note that the combination (TWD = 30°,TWS = 20 m/s) had to be discarded due to a manipulation error, so the total number of tests amounted to 20. Again, the propulsion unit was controlled to deliver a power of 3078 kW, which led to a vessel speed of 12.25 kt without rotor sails. The rudder was controlled to achieve a COG of zero. Key results for these tests are presented as polar plots in Fig. 11 where the azimuth represents the true wind direction TWD. *Note that TWD and TWA are close to each other as the ship had a COG of zero, but are not strictly equal as the ship had a non-zero yaw/drift angle. Results are presented as a function of TWD.*

From Fig. 11, the effect of the rotor sails on the vessel speed is seen to be beneficial for a wide range of wind directions from 150° to about 50°, with a maximum benefit at beam reach (TWD$\in$ [90°, 110°]), the exact optimal angle depending on the wind velocity. The maximum

Table 4
Statistical properties of key quantities for seven repetitions of the same test. Full-scale values.

	Mean	Std. dev	CoV%	Min	Max
Velocity [m/s]	7.40	0.04	0.55	7.35	7.45
Heel [°]	−0.80	0.02	2.32	−0.84	−0.78
Trim [°]	−0.16	0.01	7.98	−0.19	−0.15
Yaw/drift [°]	0.65	0.20	30.04	0.40	0.91
Rudder Angle [°]	3.91	0.10	2.52	3.82	4.10
T_p [kN]	427.24	9.34	2.19	414.31	441.22
Q_p [kNm]	447.22	3.85	0.86	442.59	454.42
n_p [Hz]	1.09	0.01	0.83	1.08	1.11
P_p [kW]	3077.10	0.45	0.01	3076.57	3077.80
$\tau_{\text{sail},1}$ [kN]	192.64	1.42	0.74	190.92	194.78
$\tau_{\text{sail},2}$ [kN]	−361.52	2.29	0.63	−364.31	−358.56
$\tau_{\text{sail},4}$ [kNm]	−6641.15	42.13	0.63	−6691.42	−6587.16
$\tau_{\text{sail},5}$ [kNm]	−3730.62	24.99	0.67	−3767.22	−3700.39
$\tau_{\text{sail},6}$ [kNm]	3381.63	21.12	0.62	3352.57	3406.94
$\tau_{\text{friction},1}$ [kN]	429.56	4.02	0.94	425.02	435.09
$\tau_{\text{roll damping},4}$ [kNm]	−0.01	0.06	n.r	−0.11	0.08
$\tau_{\text{meas},1}$ [kN]	626.49	3.88	0.62	622.29	631.83
$\tau_{\text{meas},2}$ [kN]	−367.70	3.23	0.88	−370.98	−363.22
$\tau_{\text{meas},3}$ [kN]	−150.99	1.44	0.96	−153.25	−149.19
$\tau_{\text{meas},4}$ [kNm]	−6682.75	58.26	0.87	−6741.08	−6599.87
$\tau_{\text{meas},5}$ [kNm]	−3742.35	5.24	0.14	−3750.69	−3736.18
$\tau_{\text{meas},6}$ [kNm]	3316.60	28.12	0.85	3276.51	3345.24

achieved speed was beyond 17.3 kn, which is a significant increase compared to the nominal speed of 12.25 kn, which consistent with previous studies on the subject (Tillig and Ringsberg, 2020). At this speed the fraction of the total thrust coming from the sails exceeds 60%. However the gain of speed deteriorated dramatically in close hauled conditions (TWD = 50°), and was totally lost when moving further towards head winds (TWD = 30°). The trim was not significantly affected by the sails forces (less than 0.3 deg for the range of conditions tested here). The heel angle, drift angle, and the use of rudder increased consistently when the TWD decreased. These quantities remained small

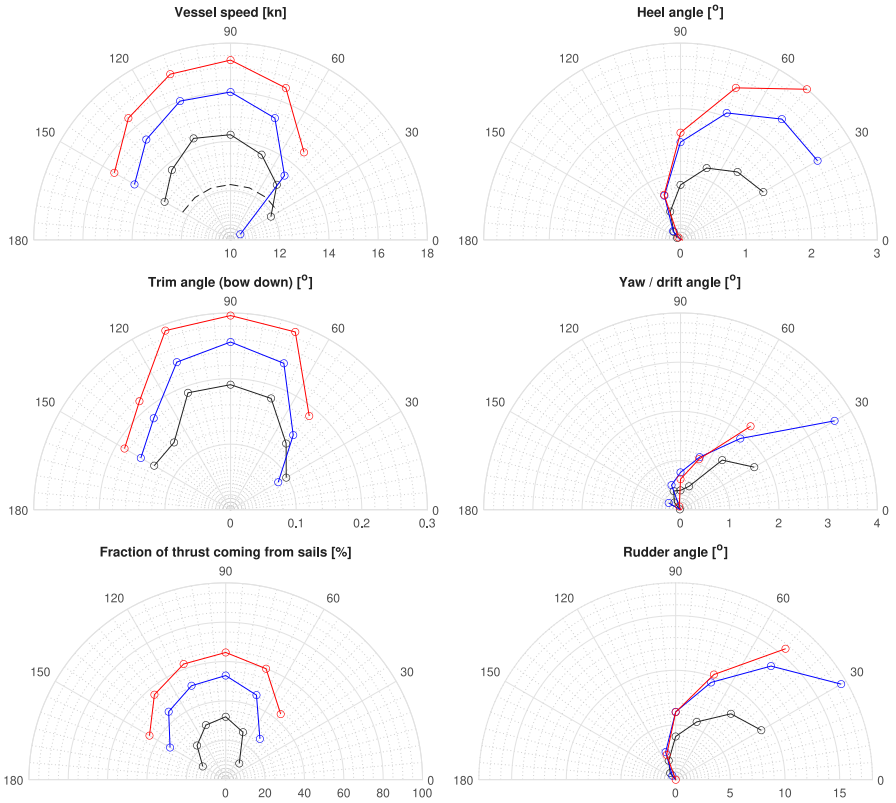

Fig. 11. Key vessel parameters as a function of the true wind direction (TWD) and true wind speed (TWS). TWS = 10, 15, 20 m/s are represented in black, blue and red, respectively. The dashed black reference line represents values for the case without Flettner rotors (speed 12.25 knots). (For interpretation of the references to color in this figure legend, the reader is referred to the web version of this article.)

for TWD> 90°, and would not matter in an operational context. They become however significant for TWD< 90°, culminating (for the tested conditions) to heel and drift angles exceeding 3 degrees, which would be noticeable for the crew, and a rudder angle exceeding 15 degrees.

To understand the mechanisms at play, loads generated by the sails are considered. Fig. 12 shows the range of apparent wind angle and wind speed (AWA and AWS) for all rotors and strips, as well as the range of lift and drag forces per unit length. On the lower part of the figure, relevant components of the sail load τ_{sail}, expressed in the vessel coordinate system $\{b\}$, are presented. Schematically, three regimes can be distinguished. (1) For close reach conditions (TWD< 70°), the apparent wind speed AWS is large, causing lift and drag forces to be at their maximum. However, at these wind directions, the large aerodynamic loads yield a strong sideways force and heeling moment on the ship, and a marginal net contribution to the propulsion. (2) In broad reach to following wind conditions (TWD> 130°), the AWS is small, leading to relatively net small sail forces, but thanks to the large AWA, both lift and drag contribute to the propulsion. For TWD exceeding 150°, the rotor sails play an insignificant role for the ship behavior. (3) The range 70^o <TWD< 130° is favorable for this ship and sail arrangement, where the combination of a between moderate AWS and sufficiently large AWA leads to significant propulsive forces without excessive sideways force and resulting moments on the hull. These observations are actually valid for most ship and sails types.

It is in order at this stage to recall some limitations of the sail model used in this cyber–physical experiment. First of all, the interaction between rotors being neglected, the results at low and high values of TWA should be interpreted with care. Furthermore, the spin ratio SR was on average 4.8 for TWS = 10 m/s, 3.2 for TWS = 15 m/s and 2.4 for TWS = 20 m/s. The largest value at which CFD analyses were performed in De Marco et al. (2016) was at SR = 3. In our setup, when SR exceeded 3, the drag and lift coefficients have been set to their value at SR = 3, namely $C_D = 3.2$ and $C_L = 7.2$. However, looking at Fig. 7, we observe that the efficiency of the sails (defined in De Marco et al. (2016) as the ratio C_L/C_D) decreases for SR>1.7. This means that the sail efficiency, and hence positive effect of the sail-assistance at TWS = 10 m/s might be overestimated.

Noteworthy, with the present rotor arrangement, the rotor sails always generated a positive yaw moment (tending to push the bow against the wind) that had to be compensated by the rudder and drift angle of the hull. A natural course of action for the designer would be to move the rotor sails slightly forward, or adopt different rotational speed on each rotors. The present empirical approach enables to investigate the effect of such modifications, by simply modifying the numerical sail model and re-running the test.

4.4. Propulsion analysis

As outlined in the introduction section, the application of wind propulsion leads to a number of effects that require development of new test and analysis procedures for evaluating ship performance. In particular, the individual propulsion factors related to thrust and resistance deduced from a propulsion analysis will as such have a different meaning than in a conventional ship propulsion test. This will be developed in this section.

We recall that the following parameters were recorded during the tests: the propeller thrust T_p, torque Q_p, rate of revolution n, the model speed V, the applied towing force for friction correction F_{Dm}, and applied thrust force from the virtual sails T_s. The three latter are the values of v^b, τ_{sail} and τ_{friction} projected along n_1, respectively. These

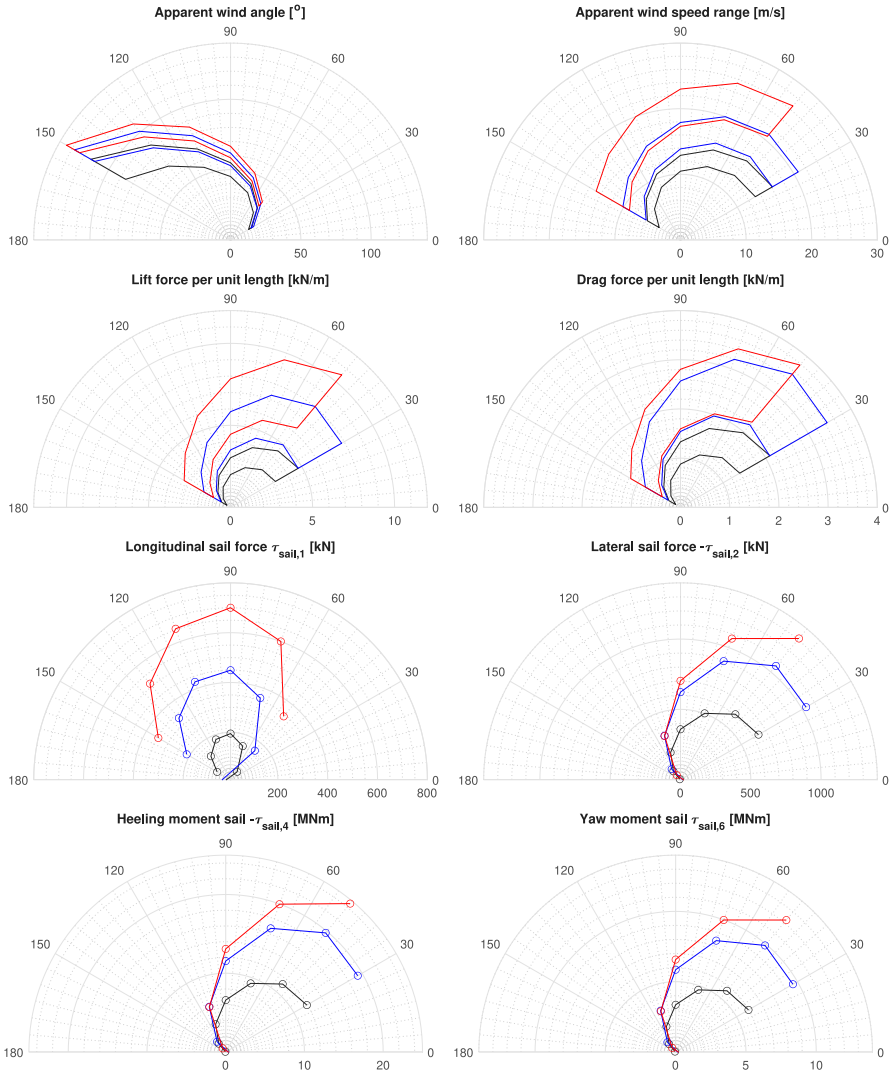

Fig. 12. Key sail parameters as a function of the true wind direction (TWD) and true wind speed (TWS). TWS = 10, 15, 20 m/s are represented in black, blue and red, respectively. (For interpretation of the references to color in this figure legend, the reader is referred to the web version of this article.)

measurements are combined with results from a conventional straight-line resistance test of the model, and an open water test of the propeller (presented in Figs. B.15 and B.16, respectively) as follows.

First, the thrust and torque measured during propulsion and open water tests are expressed in a non-dimensional form as

$$K_{T_p} = \frac{T_P}{\rho n^2 D^4} \tag{23}$$

$$K_{Q_p} = \frac{Q_p}{\rho n^2 D^5} \tag{24}$$

In the open water diagram (see Fig. B.16), K_{T_p} and K_{Q_p} are presented as functions of the advance coefficient

$$J = \frac{V}{nD} \tag{25}$$

By entering the open water diagram with the thrust coefficient measured during the free-running tests, corresponding values for J_0 and K_{Q_0}-values are obtained which are used to estimate wake fraction w.

$$w = 1 - \frac{J_0}{J} \tag{26}$$

and the relative rotative efficiency η_R

$$\eta_R = \frac{K_{Q_0}}{K_Q} \tag{27}$$

The above coefficients have the same meaning as in any conventional propulsion test, as well as the propeller efficiency in open water

$$\eta_0 = \frac{V T_p}{2\pi n Q_p} \tag{28}$$

In a classical propulsion analysis, hull efficiency η_H and quasi-propulsive coefficient η_D would then be calculated based on the thrust deduction fraction t defined as

$$t = 1 - \frac{R_{Tm} - F_{D_m}}{T_p} \tag{29}$$

where R_{Tm} is the hull resistance, obtained from dedicated resistance tests. Note that this definition refers to the model resistance in a straight-line resistance test. Under sails, sail-induced thrust should be added to the equation, redefining the thrust deduction fraction as

$$t^* = 1 - \frac{R_{Tm} - F_{Dm} - T_s}{T_p} \tag{30}$$

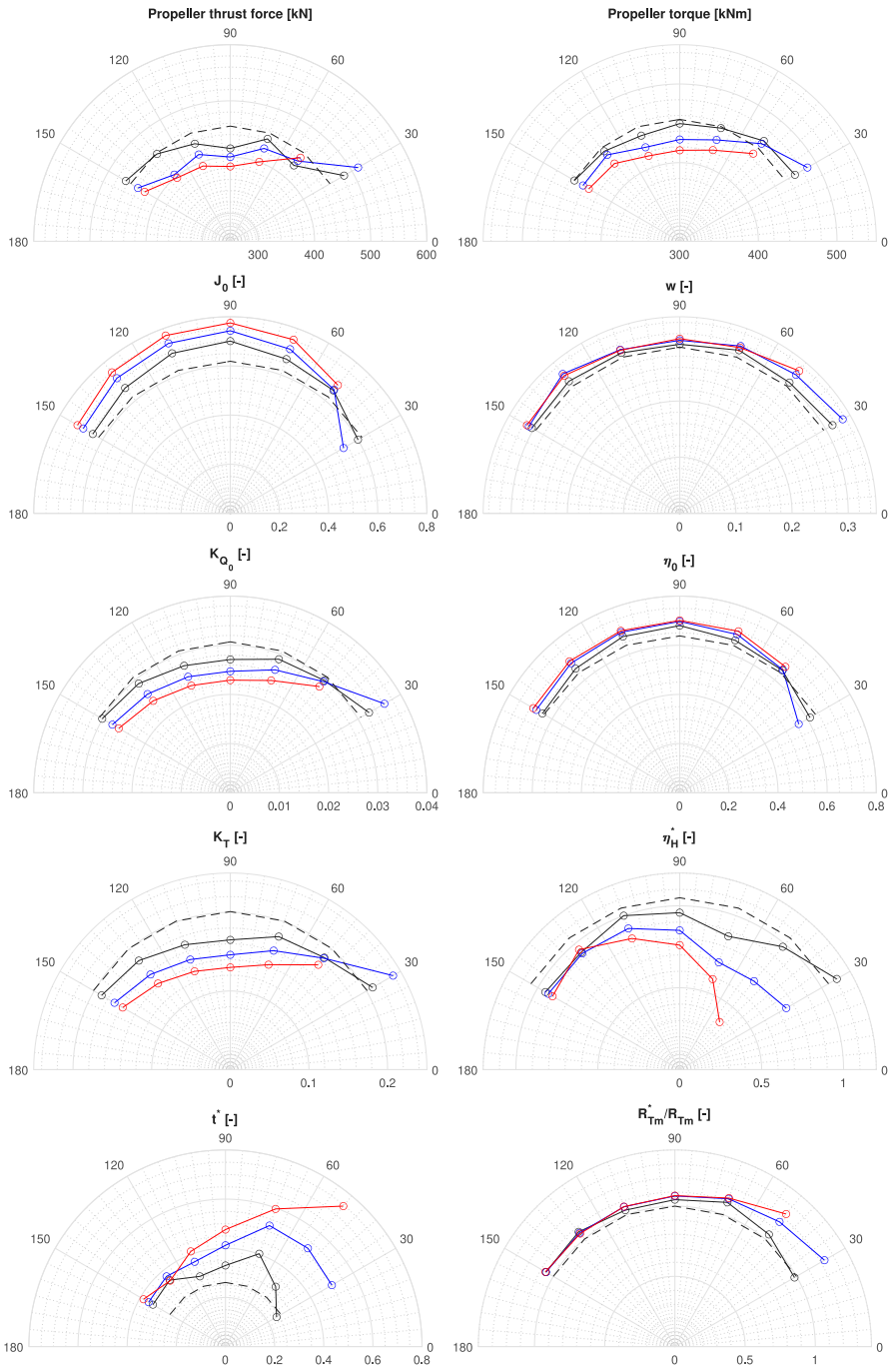

Fig. 13. Propulsion parameters as a function of the true wind direction (TWD) and true wind speed (TWS). Vessel sails towards North. TWS = 10, 15, 20 m/s are represented in black, blue and red, respectively. The dashed black reference line represents values for the case without Flettner rotors at vessel speed 12.25 knots. (For interpretation of the references to color in this figure legend, the reader is referred to the web version of this article.)

Furthermore, t^* becomes now a measure of not only the resistance increase due to the influence of the propeller, but also due to the added resistance of the hull caused by the change in running attitude (leeway and heel, and to some extent modified trim) and rudder angle, to counteract sail loads.

The hull efficiency η_H^* can then be adapted from its classical definition:

$$\eta_H^* = \frac{1 - t^*}{1 - w} \tag{31}$$

as well as the quasi-propulsive coefficient η_D^*

$$\eta_D^* = \eta_0 \, \eta_H^* \, \eta_R \tag{32}$$

The key quantities defined here are plotted in Fig. 13. It is observed that the application of virtual rotors leads to a slight increase effective wake fraction w, i.e. a slight decrease in the inflow velocity to the propeller, presumably due to a combination of introducing an oblique inflow angle, and the effect this oblique inflow has on the flow behind the skeg. The unloading of the propeller due to wind assistance is

Table A.5
a_{ijk} and b_{ijk} coefficients used in the computation of lift and drag coefficients of the rotor sails in Eqs. (9) and (10).

i	j	a_{ij1}	a_{ij2}	a_{ij3}	b_{ij1}	b_{ij2}	b_{ij3}
1	1	46.75579262	−78.30137816	20.28158198	−79.91876737	70.0714412	−15.26803135
1	2	−37.84627709	60.05841366	−15.30145164	60.03045191	−50.611248	11.01285484
1	3	8.096155602	−11.87436219	2.987144792	−11.64851051	9.810298766	−2.141092131
1	4	−0.460229167	0.639485404	−0.160067313	0.668844225	−0.557905642	0.121478361
2	1	−89.78524934	140.0099987	−35.67163964	140.7180534	−125.0475503	27.37696129
2	2	77.60674442	−112.2043683	27.97673121	−104.7031285	89.13656642	−19.29174369
2	3	−16.46077427	22.03781703	−5.408808016	20.214777	−17.09768028	3.697994054
2	4	0.915301058	−1.152095456	0.279901151	−1.155096291	0.96400734	−0.20726945
3	1	38.54701275	−62.54475786	16.26618333	−76.5057191	69.27082822	−15.18862485
3	2	−37.55599168	54.80145925	−13.70360517	57.9508028	−49.79267524	10.70937387
3	3	8.152939764	−10.75328967	2.627144928	−11.1802424	9.49315291	−2.034099935
3	4	−0.439901094	0.533754549	−0.128120357	0.63617207	−0.53087876	0.112735184
4	1	−4.895453074	8.6422211	−2.29418742	11.79866493	−10.53866427	2.289726965
4	2	5.189632047	−7.946352738	2.016174449	−9.411835208	8.064819531	−1.716103541
4	3	−1.153622261	1.555611997	−0.383202934	1.830523988	−1.54716509	0.327419112
4	4	0.060046043	−0.072807988	0.017516319	−0.103856573	0.085910493	−0.017961236

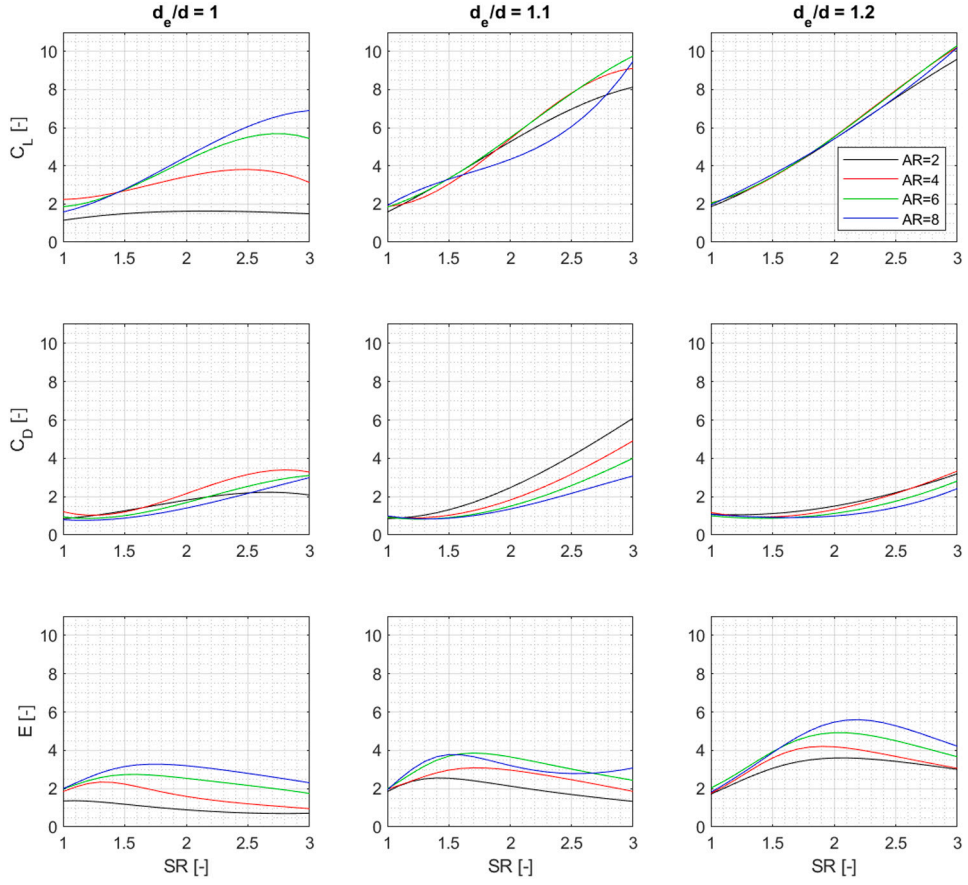

Fig. A.14. Lift and drag coefficients estimated from Eqs. (9) and (10) and Table A.5. Replication of the results presented in De Marco et al. (2016, Figure 10).

observable in the reduction in K_{T_P} and K_{Q_p} as well as in the increased advance ratio J_0 for increasing wind speeds. It is further observed that the lower propeller loading has a positive effect on the open water efficiency η_0.

Under the simplified assumption that the thrust deduction is independent of the vessel's running attitude and propeller loading, the hydrodynamic resistance of the model under influence of the virtual rotors can be approximated by

$$R^*_{Tm} = T_p(1-t) + F_{Dm} + T_s \tag{33}$$

where t is derived from the tests performed without rotors present. R^*_{Tm} is presented in Fig. 13, normalized by its counterpart when no rotors are present. As could be expected, the hydrodynamic resistance is generally increased compared to a straight-line condition, and increasingly so with increased leeway and use of rudder to maintain course. For TWD = 30° we are approaching the wind angles where the balance between negative and positive effects from the rotors shifts. At this TWD and at a TWS of 10 m/s, the net thrust from the rotors is negative, but the negative hydrodynamic effects, such as leeway, remain moderate. The attained vessel speed, propulsion factors and

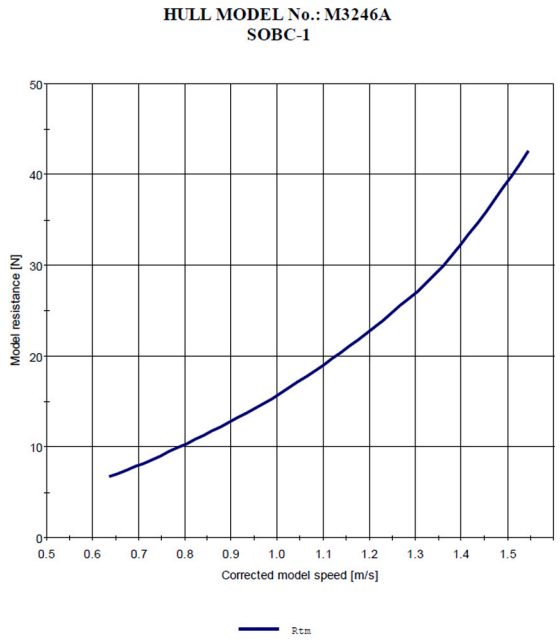

Fig. B.15. Resistance test results.

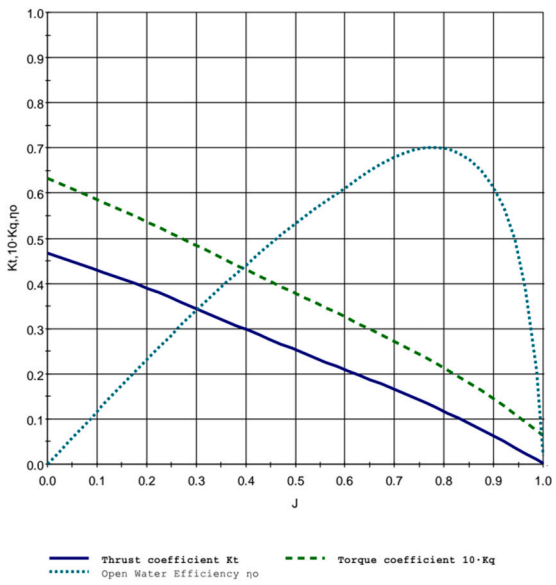

Fig. B.16. Open water test results.

estimated hull resistance approaches the case without rotors. When the TWS reaches 20 m/s, the change in apparent wind angle AWA turns the net thrust from the rotors back to positive. However, the side force and yaw moment from the rotors increase significantly, and the increased hydrodynamic resistance from yaw, heel and rudder use results in a net negative effect of the rotors on the resistance.

Another observable phenomena, recognizable for experienced sailors, is the reduced dynamics in the rudder angle for TWD = 30°/50° compared to TWD = 70°, related to the favorable effect of sailing close-hauled on the vessel's course stability.

4.5. Turbulent wind

Tests were eventually performed in turbulent (unsteady) wind modeled as described in Section 2. The text matrix combined TWD of 70°, 90°, and 110° with the three wind spectra represented in Fig. 5. The (virtual) incoming wind time series was initiated at the time the model was released from its tow lines and was freely running. Time series of quantities of interest are presented for TWD = 90° in Fig. C.19. They are representative of the ones obtained for 70° and 110°.

As it can be seen in Fig. C.19, the aerodynamic wind loads exhibited strong variations during these tests, which were applied by the CDPR as expected. This good load tracking performance was not unexpected as the maximum frequency content (at model scale) of the load was of the order of 1 Hz, which has been shown to be within the capabilities of the CDPR (Ueland et al., 2021).

The dynamical response of the vessel is not very much affected by the wind turbulence. For translational degrees of freedom, most of the frequency content of the wind loading is filtered out due to the large mass of the ship. The natural frequency in pitch is well beyond the frequency content of the wind loading meaning that the loading can be considered as quasi-static, and the water-plane area stiffness is large, meaning that this degree of freedom remains unaffected. The roll angle is the only degree of freedom that is affected, with dynamic variations of up to half a degree. Such oscillations could be noticeable for the crew in calm seas conditions, but would clearly be dominated by wave-induced roll in moderate seas. It is seen that the use of the rudder is slightly increased due to the dynamic wind load, but not in a dramatic way.

5. Conclusion

This paper reported the first free-running hydrodynamic test of a wind-assisted cargo ship with highly-controlled wind loads. The wind loads were computed from lift and drag coefficients obtained from prior CFD analyses, combined with a non-uniform and non-steady incoming wind field, and accounted for instantaneous ship kinematics. The resulting loads were applied on the ship with high precision and repeatability by a Cable Driven Parallel Robot (CDPR). The paper presented the empirical method in details, followed by a study of the SOBC-1 bulk carrier, equipped with four rotor sails running at constant rotational speed.

Variations of the vessel speed, roll angle, drift angle, and rudder use as a function of the incoming wind angle and speed were documented, and found to be qualitatively in line with previous studies of sail-assisted ships. The beneficial effect of the sails on the vessel velocity was documented for true wind angles larger than 50°. SOBC-1 being a large ship with in terms displacement and water-plane area stiffness, both static and dynamic roll were rather limited (up to 3 degrees at most). Alternative designs, with a more slender hull optimized for sailing, would experience larger roll angles. The rudder angle could be large, up to 17 degrees, when sailing close-hauled (TWA< 50°). Propulsion analyses based on standard procedures for conventional ship model propulsion indicate that the effective wake is nearly unaffected by the changes in the vessel's running attitude. Furthermore, the lighter propeller loading, induced by sail-assistance, led to a higher propeller open water efficiency. Under simplifying assumptions developed in the paper, the hydrodynamic resistance was found to increase compared to a straight-line condition, and increasingly so with increased leeway and use of rudder to maintain course. For true wind angles larger than 70°, the resistance increase remained generally within 5%–10%.

The main limitations of the present work lies in the simplistic aerodynamic model that has been used. Indeed, wind shear, sail-hull interaction, sail-sail interactions, were neglected, and the semi-empirical formula for the drag and lift coefficients of the rotor sails entailed significant uncertainties, especially at high spin ratios. It is however

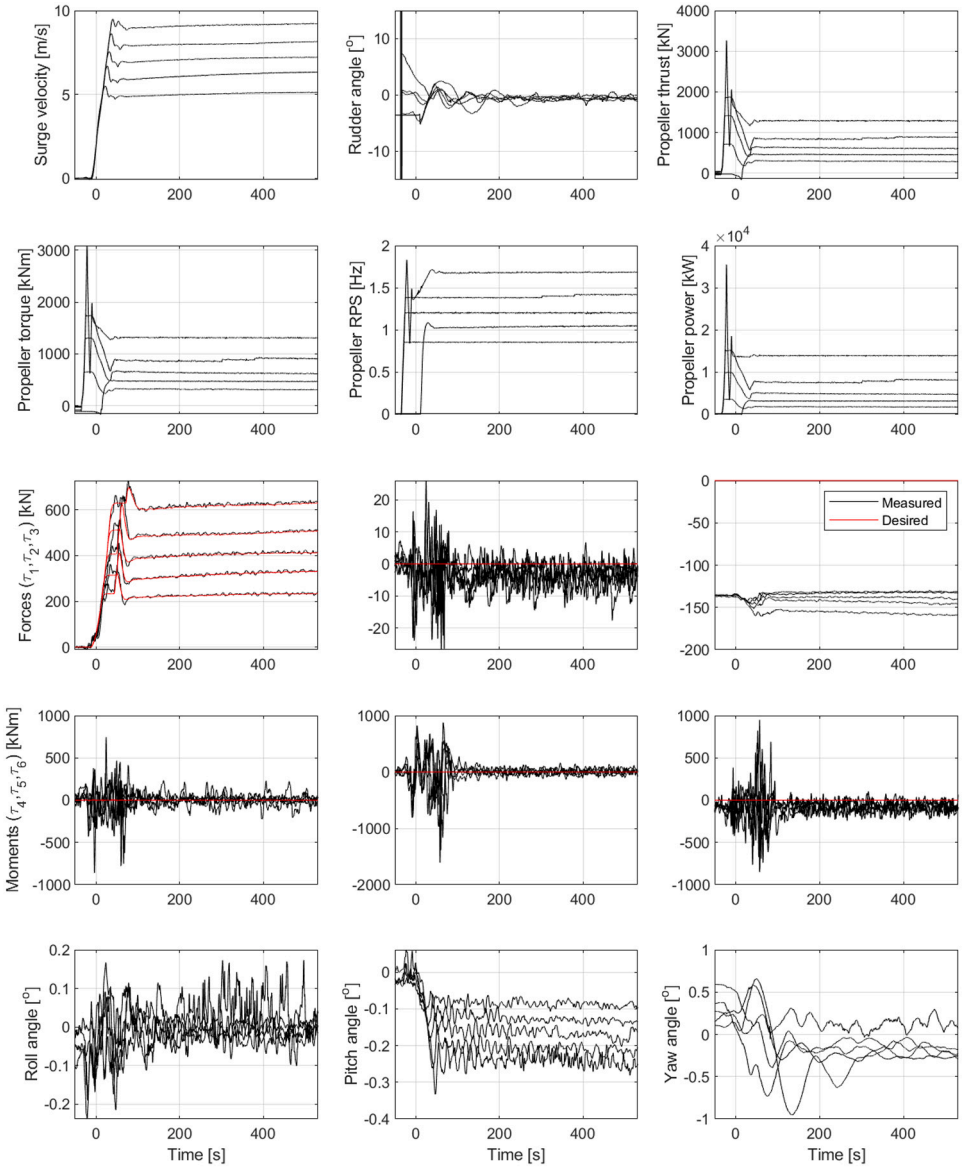

Fig. C.17. Time series of key quantities during tests without sails at different velocities (but using friction correction). Red color indicates the desired load to be applied by the CDPR. Time series were synchronized by choosing the time where the forward velocity of the vessel crosses 2 m/s (full-scale) as the time origin. (For interpretation of the references to color in this figure legend, the reader is referred to the web version of this article.)

expected that semi-empirical models of interacting sails, based on e.g. Large Eddy CFD simulations and wind-tunnel testing, will gain in accuracy in the years to come, which will benefit to the present method.

The presented empirical method is then expected to become a key element in the toolbox of designers and researchers, as radically new concepts of hulls, appendages (including e.g. centeboards, daggerboards, or novel rudder types) and propulsion systems are being proposed to exploit optimally wind assistance. The present approach enables a holistic validation of the performance of these new designs, with a focus on hydrodynamic aspects. Furthermore, such a cyber–physical approach enables rapid comparative assessments of various sail types, arrangements, or sail reefing/control strategies. Other aspects of interest that may be studied by the present method include (1) course stability under sails, (2) loss of maneuvering capabilities under sails, (3) beneficial effect of sails to damp motions in waves, and (4) consequence on added resistance in waves.

CRediT authorship contribution statement

Thomas Sauder: Conceptualization, Methodology, Software, Validation, Investigation, Data curation, Writing – original draft, Writing – review & editing, Visualization. **Sverre A. Alterskjær:** Conceptualization, Methodology, Validation, Investigation, Data curation, Writing – original draft, Writing – review & editing, Visualization, Project administration, Funding acquisition.

Declaration of competing interest

The authors declare that they have no known competing financial interests or personal relationships that could have appeared to influence the work reported in this paper.

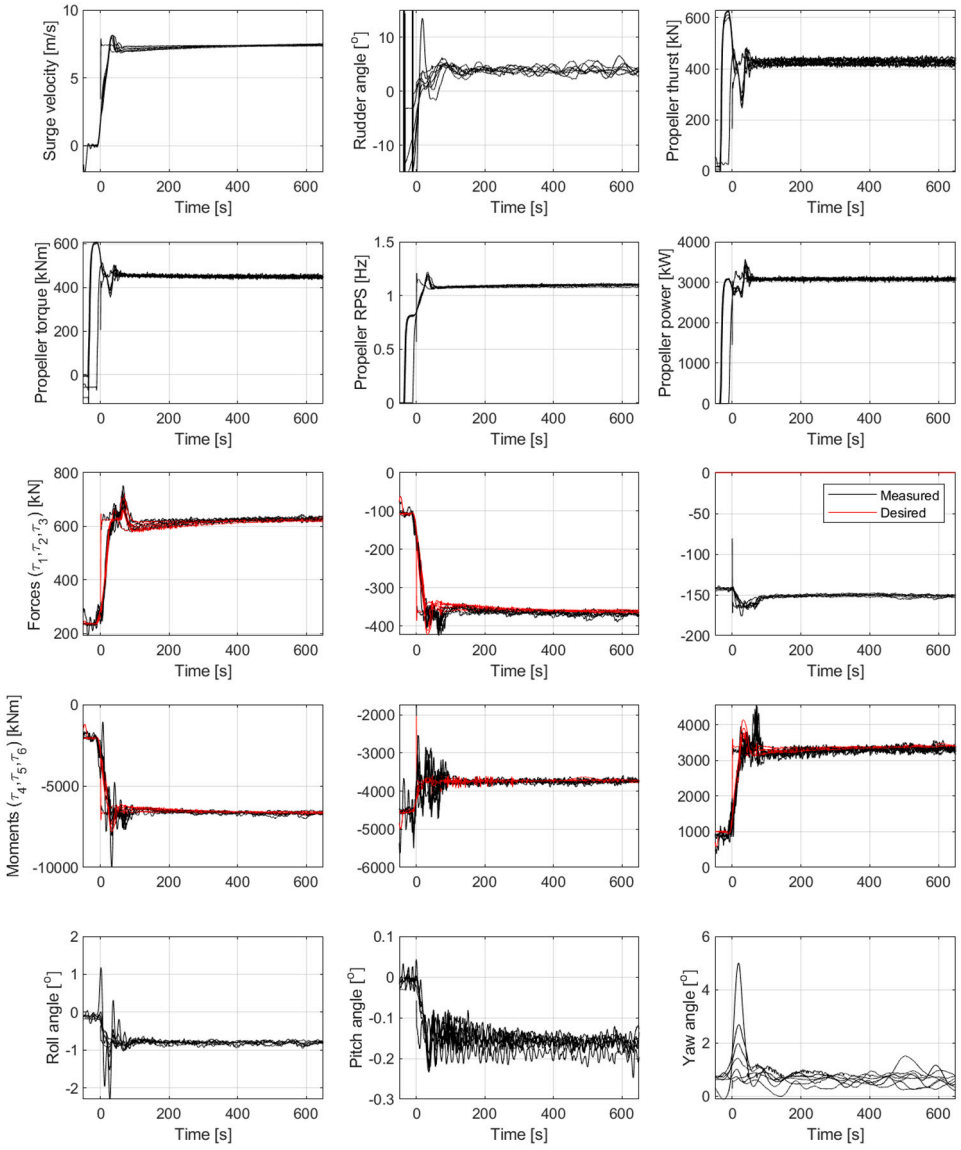

Fig. C.18. Superimposed time series for the seven (7) repetitions of the same test (TWD = 90deg, TWS = 10 m/s). See statistical properties in Table 4.

Acknowledgments

This research has been funded by the Research Council of Norway through projects 194068 and 237917. The authors would like to thank Dr. Simone Mancini for providing corrected polynomial coefficients describing the lift and drag on the rotor sail (see Table A.5). Thanks to Mrrs. Roar Reinåsdal, Arild Rabben, and Ronny Hammervik for their help in the preparation and execution of the tests. Finally, thanks to Dr. Øyvind B. Magnussen and Mr. Lars Ove Sæther, who have played a key role in the development of the autopilot, carriage steering and actuator control.

Appendix A. Surrogate model of C_L and C_D

A surrogate model of C_L and C_D as a function of AR, SR, and d_e/d was established based on CFD computations by De Marco et al. (2016). However, the polynomial coefficients reported in the original paper lack significant digits which make the surrogate model unusable. Coefficients with sufficiently high precision have been obtained in private communication with the authors, which are reported in Table A.5. See Fig. A.14 for an independent replication of De Marco et al. (2016, Figure 10) using the present set of coefficients.

Appendix B. Open water and resistance test results

See Figs. B.15 and B.16.

Appendix C. Additional figures — time series

See Figs. C.17, C.18, and C.19, referred and analyzed in the main text.

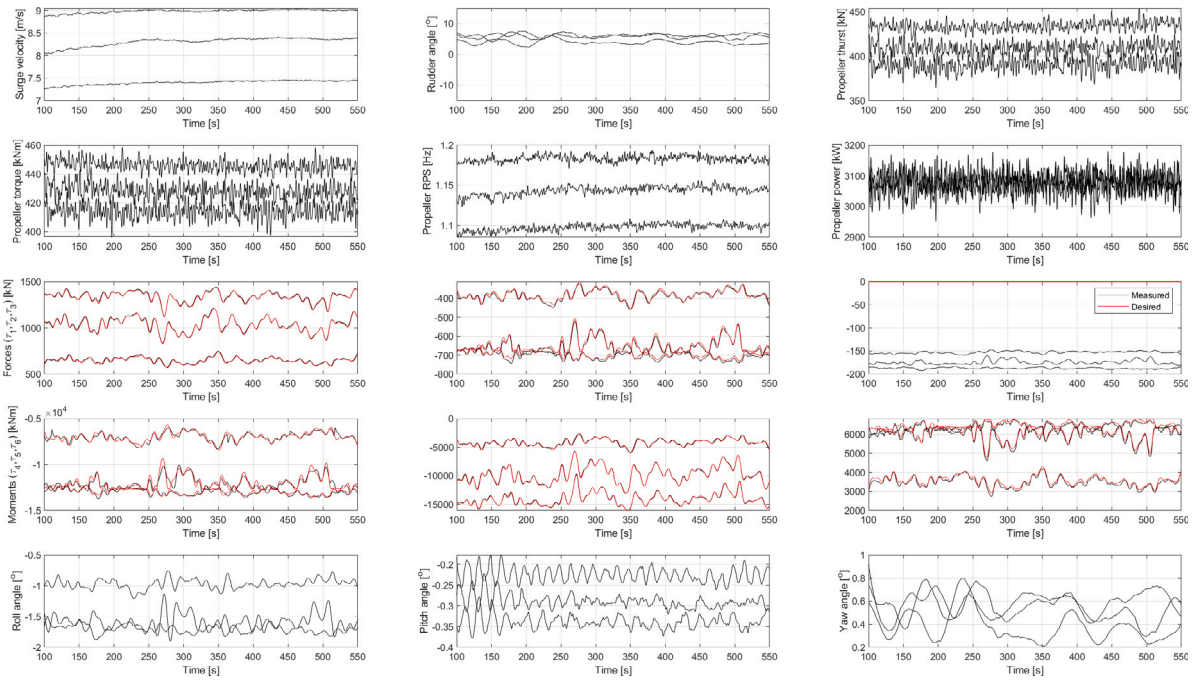

Fig. C.19. Time series of key quantities during tests in turbulent wind with TWD = 90° and the three wind spectra presented in Fig. 5.

References

Allen, C.K., Goupee, A.J., 2017. Assessment of wind/wave basin capability for emulating active blade pitch and generator control influence on floating wind turbine response. In: Proceedings of the 27th International Offshore and Polar Engineering Conference (ISOPE 2017), San Fransisco.

Anon, 2021. Centre for research based innovation (SFI) smart maritime project number 237917. http://www.smartmaritime.no/.

Bachynski, E.E., Thys, M., Chabaud, V., Sauder, T., Sæther, L.O., 2016. Real-time hybrid model testing of a braceless semi-submersible wind turbine. part II: experimental results. In: ASME 2016 35th International Conference on Ocean, Offshore and Arctic Engineering.

Bordogna, G., Muggiasca, S., Giappino, S., Belloli, M., Keuning, J., Huijsmans, R., van 't Veer, A., 2019. Experiments on a Flettner rotor at critical and supercritical Reynolds numbers. J. Wind Eng. Ind. Aerodyn. 188, 19–29. http://dx.doi.org/10.1016/j.jweia.2019.02.006.

Council of the European Union, 2015. Regulation (EU) 2015/757 of the European parliament and of the council of 29 april 2015 on the monitoring, reporting and verification of carbon dioxide emissions from maritime transport, and amending directive 2009/16/EC. Official J. Eur. Union 58, 55–76. http://dx.doi.org/10.5040/9781782258674.

De Marco, A., Mancini, S., Pensa, C., Calise, G., De Luca, F., 2016. Flettner rotor concept for marine applications: a systematic study. Int. J. Rotating Mach. 2016, 1–12. http://dx.doi.org/10.1155/2016/3458750.

Fossen, T.I., 2011. Handbook of Marine Craft Hydrodynamics and Motion Control. John Wiley & Sons, Ltd.

Garzón, F., Figueroa, A., 2017. The study on the flow generated by an array of four flettner rotors: theory and experiment. Appl. Math. 08 (12), 1851–1858. http://dx.doi.org/10.4236/am.2017.812132.

ITTC Quality System Manual, 2017. Recommended Procedures and Guidelines. Procedure 1978 ITTC Performance Prediction Method.

Kramer, J.A., Steen, S., Savio, L., 2016. Drift forces – wingsails vs flettner rotors. In: High Performance Marine Vehicles. Cortona.

Lu, R., Ringsberg, J.W., 2020. Ship energy performance study of three wind-assisted ship propulsion technologies including a parametric study of the Flettner rotor technology. Ships Offshore Struct. 15 (3), 249–258. http://dx.doi.org/10.1080/17445302.2019.1612544.

Magnus, G., 1853. Über Die Abweichung Der Geschosse, Und: Über Eine Abfallende Erscheinung Bei Rotierenden Körpern (On the deviation of projectiles, and on a sinking phenomenon among rotating bodies). Ann. Der Phys. 164 (1), 1–29.

Pearson, D.R., 2014. The use of flettner rotors in efficient ship design. In: RINA, Royal Institution of Naval Architects - Influence of EEDI on Ship Design, London, UK. pp. 162–169.

S Souza, C.E., Hegseth, J.M., Bachynski, E.E., 2020. Frequency-dependent aerodynamic damping and inertia in linearized dynamic analysis of floating wind turbines. J. Phys. Conf. Ser. 1452, 012040. http://dx.doi.org/10.1088/1742-6596/1452/1/012040.

Sauder, T., Chabaud, V., Thys, M., Bachynski, E.E., Sæther, L.O., 2016. Real-time hybrid model testing of a braceless semi-submersible wind turbine. part I: the hybrid approach. in: ASME 2016 35th International Conference on Ocean, Offshore and Arctic Engineering.

Thys, M., Chabaud, V., Sauder, T., Eliassen, L., Sæther, L.O., Magnussen, Ø.B., 2018. Real-time hybrid model testing of a semi-submersible 10 MW floating wind turbine, and advances in the test method. In: ASME 2018 1st International Offshore Wind Technical Conference, San Fransisco.

Thys, M., Souza, C., Sauder, T., Fonseca, N., Berthelsen, P.A., Engebretsen, E., Haslum, H., 2021. Experimental investigation of the coupling between aero- and hydrodynamical loads on a 12 mw semi-submersible floating wind turbine. In: Proceedings of the ASME 2021 40th International Conference on Ocean, Offshore and Arctic Engineering.

Tillig, F., Ringsberg, J.W., 2020. Design, operation and analysis of wind-assisted cargo ships. Ocean Eng. 211, 107603. http://dx.doi.org/10.1016/j.oceaneng.2020.107603.

Tokaty, 1994. A History and Philosophy of Fluid Mechanics, Reprint edition Dover Publications.

Ueland, E., Sauder, T., Skjetne, R., 2020. Optimal force allocation for overconstrained cable-driven parallel robots: continuously differentiable solutions with assessment of computational efficiency. IEEE Trans. Robot. 1–8. http://dx.doi.org/10.1109/TRO.2020.3020747.

Ueland, E., Sauder, T., Skjetne, R., 2021. Force tracking using actuated winches with position-controlled motors for use in hydrodynamical model testing. IEEE Access 1. http://dx.doi.org/10.1109/ACCESS.2021.3083539.